

# Cheap, Large-scale, and High-performance Graphite-based Flexible Thermoelectric Materials and Devices with Supernormal Industry Feasibility

*Shuai Sun, Xiao-Lei Shi, Wei-Di Liu, Ting Wu, Dezhuang Wang, Hao Wu, Xiaoyong Zhang, Yu Wang, Qingfeng Liu,\* and Zhi-Gang Chen\**

**KEYWORDS:** *thermoelectric, expanded graphite, flexible, cost-effectiveness, industrial feasibility*

**ABSTRACT:** Flexible thermoelectric materials and devices show great potentials to solve energy crisis but still face great challenges of high cost, complex fabrication, and tedious post-processing. Searching abnormal thermoelectric materials with rapid and scale-up production can significantly speed their applications. Here, we develop super large 25×20 cm<sup>2</sup> commercial-graphite produced composite films in batches, achieved by standard 10-minute industrial process. The high cost-effectiveness ( $S^2\sigma/\text{Cost}$ ) of 7250  $\mu\text{W g m}^{-1} \text{K}^{-2} \$^{-1}$  is absolutely ahead of the existing thermoelectric materials. The optimized composite film shows a high power factor of 94  $\mu\text{W m}^{-1} \text{K}^{-2}$  at 150 °C, representing the optimal value of normal carbon materials so far. Furthermore, we design two types of flexible thermoelectric devices fabricated based on such novel composite, which achieve an output open-circuit voltage of 3.70 mV using human wrist as the heat source, and 1.33 mV soaking in the river water as cold sources, respectively. Our study provides distinguished inspiration to enrich flexible and cost-effective thermoelectric materials with industry production.

# 1. INTRODUCTION

Benefited from the advantages of lightweight, portable, noise-free, and eco-friendly features,<sup>1-5</sup> flexible thermoelectric (FTE) materials and devices have exhibited great potential for applications in the areas of wearable electronics,<sup>6,7</sup> pipeline heat collection,<sup>8,9</sup> and implantable medical devices.<sup>10-12</sup> Their performance can be evaluated by the parameter of figure-of-merit  $ZT=S^2\sigma T/\kappa$ , which is determined by the absolute temperature ( $T$ ), electrical conductivity ( $\sigma$ ), Seebeck coefficient ( $S$ ), and thermal conductivity ( $\kappa$ ). The power factor  $S^2\sigma$  is another important parameter to evaluate the ability of thermopower generation.<sup>13-15</sup> Generally, there are mainly three types of FTE materials, including conductive polymers (*e.g.* PEDOT:PSS and PANI),<sup>16-18</sup> carbon-based materials (*e.g.* carbon nanotube and graphene),<sup>19,20</sup> and flexible inorganic semiconductors (*e.g.* Ag<sub>2</sub>Se and InSe).<sup>21,22</sup> However, existing FTE materials **are still suffering** from their complicated synthesis and high cost, which significantly restricts their practical applications. Due to the ubiquity of temperature gaps in human activities which will boost the practical requirements in large-scope energy conversion, it is of significance to develop **industrial** feasible FTE materials with high performance, facile fabrication, and high cost-effectiveness.<sup>23</sup>

**Among advanced carbon-based flexible thermoelectric materials, a fullerene-based film was the first-reported in 1993 with a  $S^2\sigma$  of  $2.8 \mu\text{W m}^{-1} \text{K}^{-2}$ .<sup>24</sup> Subsequently, most of the studies on carbon-based FTE materials were focused on carbon nanotubes (CNTs) and graphene.<sup>6</sup> CNTs (including single-walled carbon nanotubes SWCNTs and multi-walled carbon nanotubes MWCNTs) are featured with small diameter, large surface area, high aspect ratio, and narrow bandgap.<sup>25</sup> Sheng et al. studied**

the effects of heat treatment at different temperatures and atmospheres for pure SWCNT films to obtain a maximum  $S^2\sigma$  of  $113.7 \mu\text{W m}^{-1} \text{K}^{-2}$  at room temperature.<sup>26</sup> Choi et al. fabricated a highly-aligned CNT sheet synthesized by floating catalyst chemical vapor deposition, showing the highest  $S^2\sigma$  of  $158 \mu\text{W m}^{-1} \text{K}^{-2}$  at room temperature.<sup>27</sup> Additionally, two-dimensional graphene featured with honeycomb hexagonal planar structures consisting of sp<sup>2</sup> hybridized carbon atoms is widely used in thermoelectric areas.<sup>20</sup> Miao's team has prepared tellurium nanowires and RGO double-layer composite film has exhibited a  $S^2\sigma$  of  $80 \mu\text{W m}^{-1} \text{K}^{-2}$  because of the energy filtering effect.<sup>28</sup> Novak et al. provided a new strategy to prepare n-type graphene films via non-oxidative intercalation and molecular adsorption method. An extremely high  $S^2\sigma$  of  $673 \mu\text{W m}^{-1} \text{K}^{-2}$  has been reached.<sup>29</sup> However, the synthesis methods of these advanced carbon thermoelectrics are still complex, high cost, and high energy consumption.

Conventional carbon **material refers** to the industrial classifications, such as graphite, carbon black, carbon fiber, expanded graphite, and graphite intercalation on compounds.<sup>30,31</sup> These materials are commercially available. Especially, worm-like expanded graphite (EG) exhibits excellent flexibility and **considerable** molding potentials, which is commonly fabricated by intercalation, washing, drying, and high-temperature expansion of natural graphite films in order.<sup>32</sup> Graphite intercalation on compounds (GIC) is formed by inserting chemical reagents into graphite layers, which can decompose and release gases after heat treatments to distend the layer spacing.<sup>33</sup> The most commonly used commercial **intercalated** reagents are concentrated sulfuric acid, hydrogen peroxide, and nitric acid.<sup>34,35</sup> However, till now, **conventional** carbon materials are rarely picked as thermoelectric components due to their inadequate thermoelectric performance as illustrated in **Figure 1a** and **Table S1**.<sup>36</sup> Wei *et al.* reported a record high  $S^2\sigma$  of  $94 \mu\text{W m}^{-1} \text{K}^{-2}$  for the expanded graphite composite at 72 °C by filling with 3 wt% ionic liquids.<sup>37</sup> However, the **value of**  $S^2\sigma$  dropped by 140

folds to  $0.67 \mu\text{W m}^{-1} \text{K}^{-2}$  at ambient temperature. Besides, FTE devices totally composed of conventional carbon materials have not been reported so far.

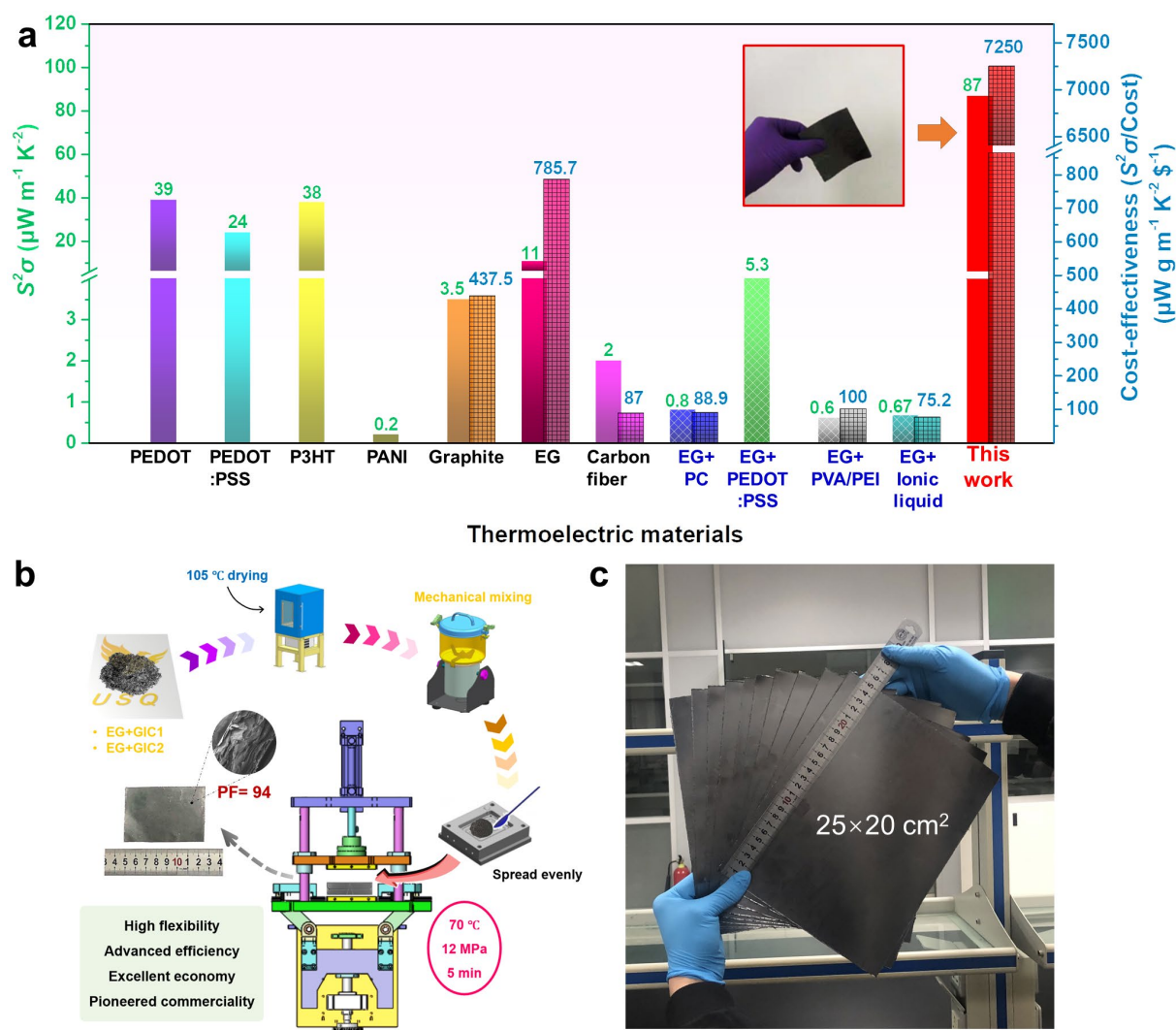


**Figure 1.** (a) Comparison of the room temperature power factors and calculated cost-effectiveness ( $S^2\sigma/\text{Cost}$ ) of EG<sub>3</sub>-GIC<sub>27</sub> (this work) with other representative flexible thermoelectric materials including organic polymers, pure EG and EG/polymer blends, (b) Schematic diagram showing the synthesis process of EG-GIC compounds, and (c) Large-scale fabricated EG<sub>3</sub>-GIC<sub>27</sub> composite thin films. Note: as for the designation, the pure EG, GIC1 (170 mesh), GIC2 (90 mesh), and their composites were named in accordance with their prescriptions. For example, EG<sub>3</sub>-GIC<sub>27</sub> refers to that the compounding ratio of EG and GIC2 is 3:7 (wt:wt).

In this work, we develop an effective EG-GIC composite with both high performance and high cost-effectiveness. One of the most significant highlights is that all raw materials used in this work are commercially available, and can be one-step fabricated into the target thermoelectric materials by a typical industrial hot-pressing method.<sup>38-40</sup> This EG-GIC system was elaborately selected by comparison of large amount of preliminary experiment results as shown in **Table S2** and **Table S3**. The thickness of the fabricated thin film was controlled at around 0.3 mm to ensure high flexibility, and the in-plane size can reach as large as 25×20 cm<sup>2</sup> (**Figure 1c**), which is likely to be further expanded by large-scale industrial molds. Notably, the entire preparation process can be cycled once in 10 minutes. Ten pieces of volume products are acquired for demonstration as shown in **Figure 1c**, offering great industrial operability. Characterization results show that the EG-GIC combination with larger particle size gaps can result in better thermoelectric performance. The maximum  $S^2\sigma$  can reach 94  $\mu\text{W m}^{-1} \text{K}^{-2}$  at 150 °C when the amount of EG is optimized at 30 wt%. Particularly, the room-temperature  $S^2\sigma$  of 87  $\mu\text{W m}^{-1} \text{K}^{-2}$  and the cost-effectiveness ( $S^2\sigma/\text{Cost}$  value of 7250  $\mu\text{W g m}^{-1} \text{K}^{-2} \text{\$}^{-1}$ ) of the as-prepared material is superior to most of the representative flexible thermoelectrics including organic polymers and modified inorganic hybrids (**Figure 1a** and **Table S1**). Besides, a homemade device using poly(ethylene terephthalate) (PET) as the substrate is prepared to harvest human wrist heat, which can generate 3.70 mV output open-circuit voltage under a temperature difference ( $\Delta T$ ) of 3.9 °C. Another homemade device using silica gel as encapsulation unit characterizes with highly transparent and self-adhesive properties, where output open-circuit voltage can reach 0.65 mV sticking on the cellphone ( $\Delta T = 0.4$  °C) and 1.33 mV submerging in the river water ( $\Delta T = 1.6$  °C).

## 2. RESULTS AND DISCUSSION

**2.1. Thermoelectric properties and structure characterizations of the EG-GIC composites.** As has been mentioned above, we have detected a large amount of commercial carbon based materials as shown in **Table S2** and **Table S3**. The EG-GIC system was reasonably picked in this work because of the highest thermoelectric performance. In order to evaluate the specific thermoelectric performance of the EG-GIC composite films with different ratios of EG:GIC,  $\sigma$ ,  $S$ , and  $S^2\sigma$  were measured, as shown in **Figure 2a-c** (vertical thermal conductivities are listed in **Figure S1**). **Figure 2a** and **Figure 2b** present the as-achieved  $\sigma$  and  $S$  as a function of EG:GIC ratio. Pure EG exhibits the highest  $\sigma$  of 1300 S cm<sup>-1</sup> but a poor  $S$  of 7.3  $\mu$ V K<sup>-1</sup>, while pure GIC exhibits the highest  $S$  of 28.5 and 25.1  $\mu$ V K<sup>-1</sup> for GIC1 and GIC2. However, both GIC1 and GIC2 exhibit low  $\sigma$  (706 and 524 S cm<sup>-1</sup>). Such property distinction is because that expanded layer-structured EG possesses excellent formability and pressure-caused compactness, which induces high  $\sigma$ . However, granular GICs form relatively fragile films after pressing with interspaces between particles, resulting in low  $\sigma$ , while the intercalation agents, such as sulfuric acid and nitric acid, are likely to arouse high  $S$ .<sup>37,41</sup> Moreover, the performance difference between GIC1 and GIC2 is caused by the different content of **intercalated** sulfuric acid and nitric acid. To optimize the thermoelectric performance, an optimal ratio of EG:GIC should be tuned to couple the  $S$  and  $\sigma$ , as plotted in **Figure 2c**. When the GIC1 content is 80 % (namely EG<sub>2</sub>-GIC<sub>18</sub>) for the EG-GIC1 system,  $S^2\sigma$  can reach its peak value of 75  $\mu$ W m<sup>-1</sup> K<sup>-2</sup>. **Further**, EG<sub>3</sub>-GIC<sub>27</sub> exhibits a higher  $S^2\sigma$  value of 87  $\mu$ W m<sup>-1</sup> K<sup>-2</sup>, which is superior compared to many reported organic polymers and conventional inorganic carbon materials, as summarized in **Table S1** in the Supporting Information. Therefore, EG<sub>3</sub>-GIC<sub>27</sub> is a promising hybrid material that is suitable as a base matrix component.

We further used **the** blade shredder to mechanically mix EG and GIC powders. To confirm

whether the rotating blades have destroyed the particle size of the raw materials, their particle size distributions were measured and presented in **Figure 2d**. Here, pure EG, GIC1, and GIC2 were measured directly, while EG<sub>2</sub>-GIC<sub>18</sub> and EG<sub>3</sub>-GIC<sub>27</sub> were characterized after the procedure of mechanical mixing. As shown in **Figure 2d**, the **primary peak** of EG particles locates at 132  $\mu\text{m}$  and the second peak appears at 280  $\mu\text{m}$ , which is attributed to the length and width anisotropy of the worm-like particle appearance.<sup>42</sup> More importantly, the majority particle sizes of GIC1 and EG<sub>2</sub>-GIC<sub>18</sub> distribute at 143 and 158  $\mu\text{m}$ . Likewise, GIC2 and EG<sub>3</sub>-GIC<sub>27</sub> display peak particle size values at 427 and 435  $\mu\text{m}$ . Besides, the emerging tail of EG<sub>2</sub>-GIC<sub>18</sub> at 480  $\mu\text{m}$  compared with GIC1 coincides with the broad EG distribution peak. The additional peak at  $\sim 132$   $\mu\text{m}$  of EG<sub>3</sub>-GIC<sub>27</sub> compared with GIC2 also matches the primary peak of pure EG. As a result, **mechanical mixing by the blade shredder have not further smash the composite both GIC and EG**, which exhibits merely mixture effects. **Figure 2d** indicates that pure EG and GIC2 possess a larger gap of grain size as raw materials that smaller EG can replenish into the interspaces of GIC2 particles. This interval filling effect results in superior material morphology and thermoelectric properties for EG-GIC2 composites compared with EG-GIC1,<sup>43</sup> which will be further discussed lately.

To investigate the lattice defects of the hybrid films, Raman spectra were performed and shown in **Figure 2e**. The characteristic peaks of pure EG, GICs, and their composites are all identical with the reported typical carbon materials. Specifically, the G bands appear at  $\sim 1580$   $\text{cm}^{-1}$ , representing the lattice order and integrity; whereas the D bands within a range of 1345 to 1359  $\text{cm}^{-1}$  (**Table S4**) are caused by the disordered crystal structures and lattice defects.<sup>44</sup> Generally, the intensity ratio  $I_D/I_G$  is defined as an important parameter to certify the lattice defect densities of carbon materials.<sup>45</sup> As shown in **Table S4**, GICs perform a higher defect level than EG, and the composites exhibit further increasing

defect degrees, which is mainly caused by the acid corrosions under 70 °C hot-pressing.<sup>46</sup> Reasonably, lattice defects decrease carrier concentrations and are beneficial to the improvement of  $S$ ,<sup>47</sup> which is corresponding with the results shown in **Figure 2b**. Additionally, reasonable intensive peak intensities of G bands compared with G' bands confirm that all specimens are multi-layered structures.<sup>48</sup>

The crystallization behaviors were studied by the X-ray diffraction (XRD) patterns, as shown in **Figure 2f**. It can be seen that pure EG, GICs, and their composites are completely crystallized, evidenced by the sharp and intense diffraction peaks. Characteristic peaks located at 26.6° and 54.7° are assigned to the (002) and (004) planes.<sup>49-51</sup> According to the Bragg equation, interlayer distances ( $d$ ) of GIC1, GIC2, EG<sub>2</sub>-GIC1<sub>8</sub>, and EG<sub>3</sub>-GIC2<sub>7</sub> were calculated to be 0.3348 ( $2\theta = 26.60^\circ$ ), 0.3346 ( $2\theta = 26.62^\circ$ ), 0.3343 ( $2\theta = 26.64^\circ$ ), and 0.3341 ( $2\theta = 26.66^\circ$ ) nm (**Figure S2**).<sup>52</sup> However, pure EG exhibits a much higher  $d$  of 0.3358 nm ( $2\theta = 26.52^\circ$ ), which confirms that the interlayer spacing of expanded graphite has been dilated. Besides, the thinner lattice interlayer distances of EG<sub>2</sub>-GIC1<sub>8</sub> and EG<sub>3</sub>-GIC2<sub>7</sub> are mainly caused by the 12 MPa pressure provided by the flat vulcanizer during the fabrication process (**Figure 1b**).

Elemental compositions of EG, GICs, EG<sub>2</sub>-GIC1<sub>8</sub>, and EG<sub>3</sub>-GIC2<sub>7</sub> are determined by X-ray photoelectron spectroscopy (XPS), as shown in **Figure 2g**. It can be seen that carbon and oxygen are the main elements for all specimens.<sup>43</sup> As well, obvious characteristic peaks of N1s and S2p confirm the introduction of NO<sub>3</sub><sup>-</sup> and SO<sub>4</sub><sup>2-</sup> to GICs, which ought to be further introduced to EG-GIC composites. Relevant specific element content ratios are listed in **Table S5**. Apparently, pure EG is primarily consists of C (96.57 %), which is decreased to 71.62 and 75.55 % for GIC1 and GIC2. Besides, higher content ratios of N and S are observed in GIC1 compared with GIC2. This is mainly due to the smaller average particle size of GIC1, leading to larger specific surface areas and inter-layer

areas. Thus, the concentrated sulfuric acid and concentrated nitric acid absorptions are more sufficient. Notably, EG<sub>2</sub>-GIC<sub>18</sub> and EG<sub>3</sub>-GIC<sub>27</sub> compounded by EG and GICs show balanced contents between pure EG and GICs but closer to EG, which proves the enriching of EG on the sample surfaces. **Figure 2h** is an enlarged perspective of XPS C1s spectra. In comparison, characteristic peaks of GICs shift to higher binding energy areas, which is caused by the increased oxidation state of C atoms after the concentrated acid treatment.<sup>53,54</sup> Likewise, GIC1 shows an obvious shift corresponding to the higher N and S contents representing the degree of acid intercalated. EG<sub>2</sub>-GIC<sub>18</sub> and EG<sub>3</sub>-GIC<sub>27</sub> also exhibit peak combinations of EG and GICs in aspects of binding energy, where a deviation to the EG trait appears at the same time. Besides, **Figure 2i** shows thermal gravimetric analysis (TGA) curves of EG-GIC composites, indicating that the thermal stability (gravimetric rate < 0.5 %) of both EG<sub>2</sub>-GIC<sub>18</sub> and EG<sub>3</sub>-GIC<sub>27</sub> maintains at a temperature up to 150 °C, confirming no expansion of the GICs.

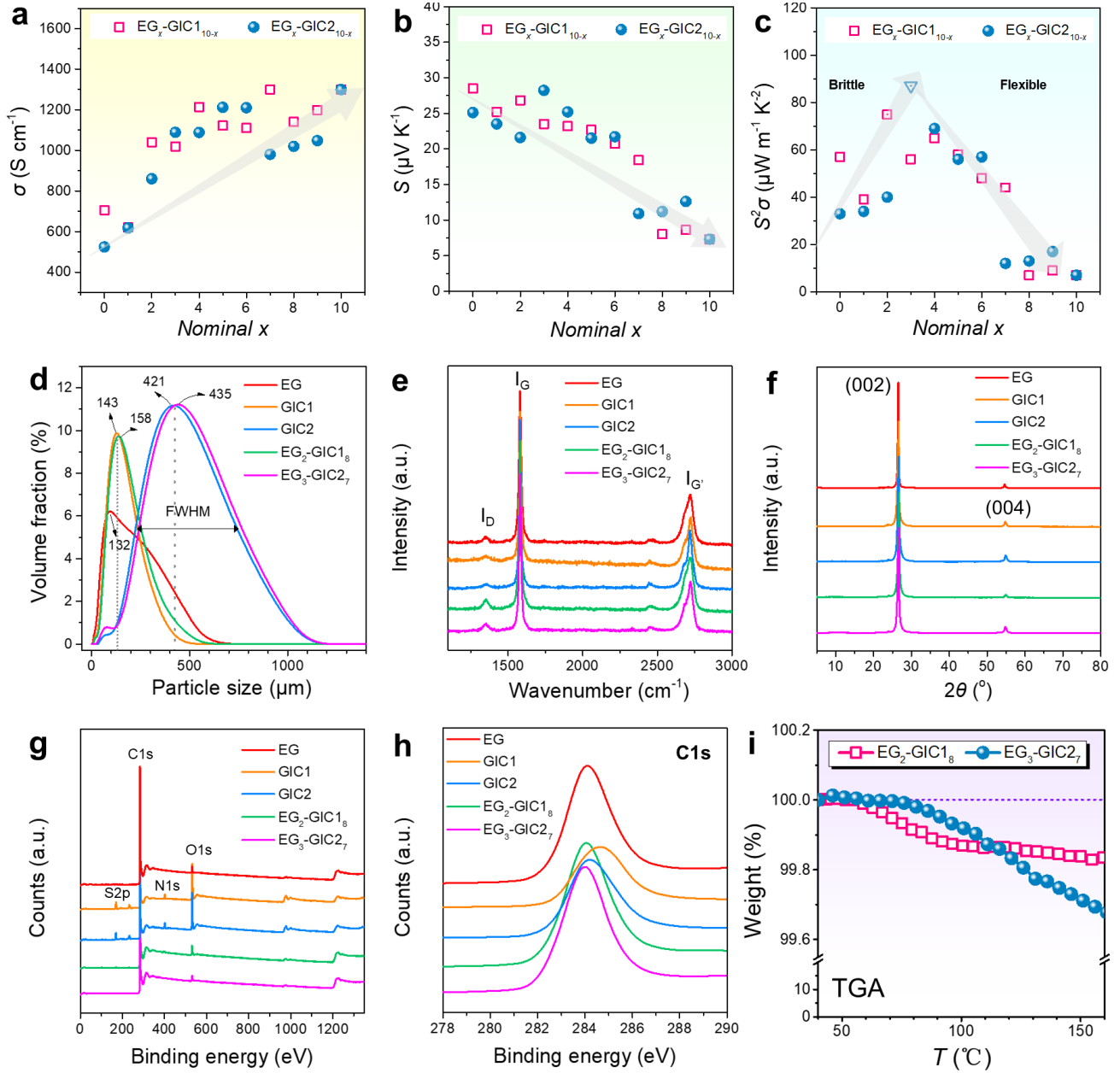


**Figure 2.** (a-c) Thermoelectric properties of electrical conductivity,  $\sigma$ , Seebeck coefficient,  $S$  and power factor,  $S^2\sigma$ . (d) Particle size distributions, (e) Raman pattern, (f) X-ray diffraction (XRD) pattern, (g-h) X-ray photoelectron spectroscopy (XPS) patterns of EG, GICs, and EG-GIC composites, and (i) thermal gravimetric analysis (TGA) curves of EG-GIC composites.

**2.2. Morphology of the EG-GIC composites.** To visually compare the compound consequents and the structural integrities, the fracture cross-sections of EG-GIC1 and EG-GIC2 composites were investigated by the scanning electron microscopy (SEM). **Figure 3a** and **Figure 3b** presents the fracture morphologies of EG<sub>2</sub>-GIC<sub>18</sub> and EG<sub>3</sub>-GIC<sub>27</sub> films, which consistently exhibit irregular multi-layered structures. Compared with EG<sub>3</sub>-GIC<sub>27</sub>, EG<sub>2</sub>-GIC<sub>18</sub> is found to show more deformed regions. Apparently, plenty of uncompact areas and deep intervals can be observed in **Figure 3a**, indicating the poor compound efficiency of EG<sub>2</sub>-GIC<sub>18</sub>. Oppositely, the layered morphology of EG<sub>3</sub>-GIC<sub>27</sub> is more consummate (**Figure 3b**), showing rare cross-surface defects. **Figure 3c** is a magnified SEM image of EG<sub>3</sub>-GIC<sub>27</sub>, where secondary layered structure appears in a thick primary layer obtained exactly in **Figure 3b**. Moreover, energy-dispersive X-ray spectroscopy (EDS) mapping results confirm the element distribution (C, O, and S) uniformity after hybridization (**Figure 3d and 3e**). **Figure 3f** shows the schematic diagram of EG-GIC composite components utilizing EG<sub>3</sub>-GIC<sub>27</sub> as a template. As illustrated in **Figure 2d**, GIC2 possesses a larger average particle size (421 μm) relative to EG (132 μm). As a result, EG particles are embedded into the gaps of the GIC matrix to fulfill the subject vacancy.<sup>43,55</sup> Thus, EG, GIC, and conductive ions (NO<sub>3</sub><sup>-</sup> and SO<sub>4</sub><sup>2-</sup>) constitute complete conductive paths,<sup>56</sup> as indicated in **Figure 3f**. The aforementioned thermoelectric properties in **Figure 2a-c** can also be explained by this model. Slight undersized EG grains raise a **full-filling** effect into the GIC matrix that is beneficial to the improvement of the thermoelectric performances (improved  $\sigma$  and  $S^2\sigma$ ).

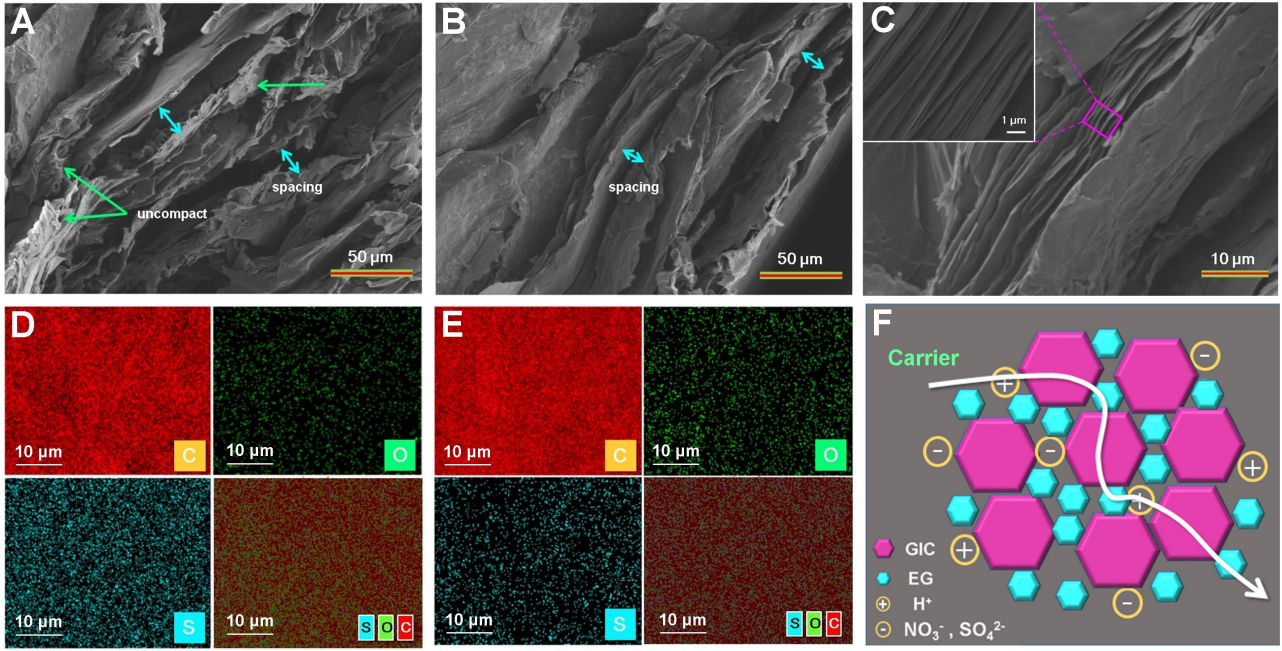


**Figure 3.** Scanning electron microscopy (SEM) images of (a) EG<sub>2</sub>-GIC<sub>18</sub>, (b-c) EG<sub>3</sub>-GIC<sub>27</sub>, EDS mapping images of (d) EG<sub>2</sub>-GIC<sub>18</sub>, (e) EG<sub>3</sub>-GIC<sub>27</sub>, and (f) Schematic illustration of carrier transport in EG-GIC composites.

### 2.3. Thermoelectric and mechanical properties under variable temperature and bending conditions.

The temperature-dependent thermoelectric properties ( $\sigma$ ,  $S$ , and  $S^2\sigma$ ) of the as-prepared EG<sub>2</sub>-GIC<sub>18</sub> and EG<sub>3</sub>-GIC<sub>27</sub> were further investigated and results are shown in **Figure 4a-c** (vertical temperature-dependent thermal conductivities are listed in **Figure S3**). With increasing the temperature up to 150 °C, both EG<sub>2</sub>-GIC<sub>18</sub> and EG<sub>3</sub>-GIC<sub>27</sub> which have been proved to be stable in **Figure 2i** display improved  $\sigma$ . Interestingly, EG<sub>2</sub>-GIC<sub>18</sub> exhibits slightly increased  $S$  from 25.6 to 26.9  $\mu\text{V K}^{-1}$ , whereas the  $S$  value of EG<sub>3</sub>-GIC<sub>27</sub> maintains nearly constant at 28.2  $\mu\text{V K}^{-1}$  (**Figure 4b**). Consequently, higher  $S^2\sigma$  can be achieved at higher temperatures for both EG<sub>2</sub>-GIC<sub>18</sub> and EG<sub>3</sub>-GIC<sub>27</sub>. A maximum  $S^2\sigma$  value of 94  $\mu\text{W m}^{-1} \text{K}^{-2}$  can be obtained at 150 °C as for EG<sub>3</sub>-GIC<sub>27</sub> (**Figure 4c**).

Moreover, **considerable** thermoelectric stability is obtained as shown in **Figure S4**. The  $S^2\sigma$  value of EG<sub>3</sub>-GIC<sub>27</sub> maintains at 71  $\mu\text{W m}^{-1} \text{K}^{-2}$  at room temperature after exposed in the air for 180 days, whereas metal alloys are prone to oxidation and organic polymer flexible films must be stored in vacuum.<sup>57-59</sup>

In addition to the high thermoelectric performance, our as-designed hybrid films also show excellent flexibilities. The flexibilities of the EG-GIC composites were measured to verify their practicality as a wearable thermoelectric material. Tensile curves are primarily described in **Figure 4d**, where specific tensile strengths and elongations are provided in **Table 1**. As can be seen, EG<sub>3</sub>-GIC<sub>27</sub> achieves superior tensile strength (0.68 MPa) and elongation (0.84 %) than EG<sub>2</sub>-GIC<sub>18</sub> which shows 0.56 MPa and 0.48 % correspondingly. Photographs in **Figure 4d** further demonstrate the as-prepared EG<sub>3</sub>-GIC<sub>27</sub> film crimping on a steel pipe with a radius of 0.9 mm.<sup>11</sup> The flexibility of EG<sub>3</sub>-GIC<sub>27</sub> film verifies that it can be qualified as a flexible thermoelectric material. Other photographs that show the arbitrary shaping of the EG<sub>3</sub>-GIC<sub>27</sub> thin film are given in **Figure S5**.

**Table 1.** Tensile strength, elongation, and elastic modulus of EG-GIC composites.

Sample	Tensile strength (MPa)	Elongation (%)	Elastic modulus (GPa)
EG <sub>2</sub> -GIC <sub>18</sub>	0.56	0.48	1.45
EG <sub>3</sub> -GIC <sub>27</sub>	0.68	0.84	0.85

In order to further evaluate the flexibility of our composites, relative electrical resistance ( $R/R_0$ ) of EG<sub>2</sub>-GIC<sub>18</sub> and EG<sub>3</sub>-GIC<sub>27</sub> were further detected under varying bending ratios, as plotted in **Figure**

**4e.** Unexpectedly, the value of  $R/R_0$  decreases gradually from 100 % to 49 % regarding EG<sub>3</sub>-GIC<sub>27</sub>. In contrast, EG<sub>2</sub>-GIC<sub>18</sub> displays an opposite upward trend from 100 % to 120 %, which snaps once the bending ratio exceeds 20 %. The feasible reason for the electric resistance decrease is proposed in the embedded graph of **Figure 4e**. During blending, the microscopic layered structures gradually approach to adjacent layers resulting in much denser blocks. Thus,  $\sigma$  can be improved when the EG<sub>3</sub>-GIC<sub>27</sub> composite film is bent and kept in an arched shape. On the contrary, tiny cracks emerge with increasing bending ratios and develop into a fracture when the bending ratio reaches 20 % for EG<sub>2</sub>-GIC<sub>18</sub> (**Figure 4d**).

**Aiming at** examine the possibility of bending signal detection of our composites, electrical resistance ( $R$ ) of EG<sub>3</sub>-GIC<sub>27</sub> were measured under varies bending cycles. Interestingly, it is found that EG<sub>3</sub>-GIC<sub>27</sub> displays the impulse resistance trend during 10 bending cycles where bending ratios of all cycles were kept at 30 %, as shown in **Figure 4f**. **Resistance of EG<sub>3</sub>-GIC<sub>27</sub> drops in the bent state compared with the original state. During 10 bending cycles, the bent resistance declines gradually as the bending time increases, which flattens out after nearly 8 cycles.** Consistent with the aforementioned bending model, the resistance in the bending **state** is generally lower than the original **state** (see the inserted images). Thus, the impulse pattern is formed during the repeated bending and stretching cycles.<sup>60</sup> **Additionally, when the EG<sub>3</sub>-GIC<sub>27</sub> film was stretched right after bending, resistance partially recovered. However, after maintaining at the stretched state for 1 min, resistance fully recovered and held for the following 5 min. Thermoelectric properties of the EG<sub>3</sub>-GIC<sub>27</sub> film were not seriously damaged after 10 cycles, which shows a  $S^2\sigma$  value of 72.60  $\mu\text{W m}^{-1} \text{K}^{-2}$  (**Table S6**). As the bending degree and bending time increase,  $\kappa$  is decreased (**Table S7**) while  $n$  maintains stable after different bending cycles (**Table S8**).**

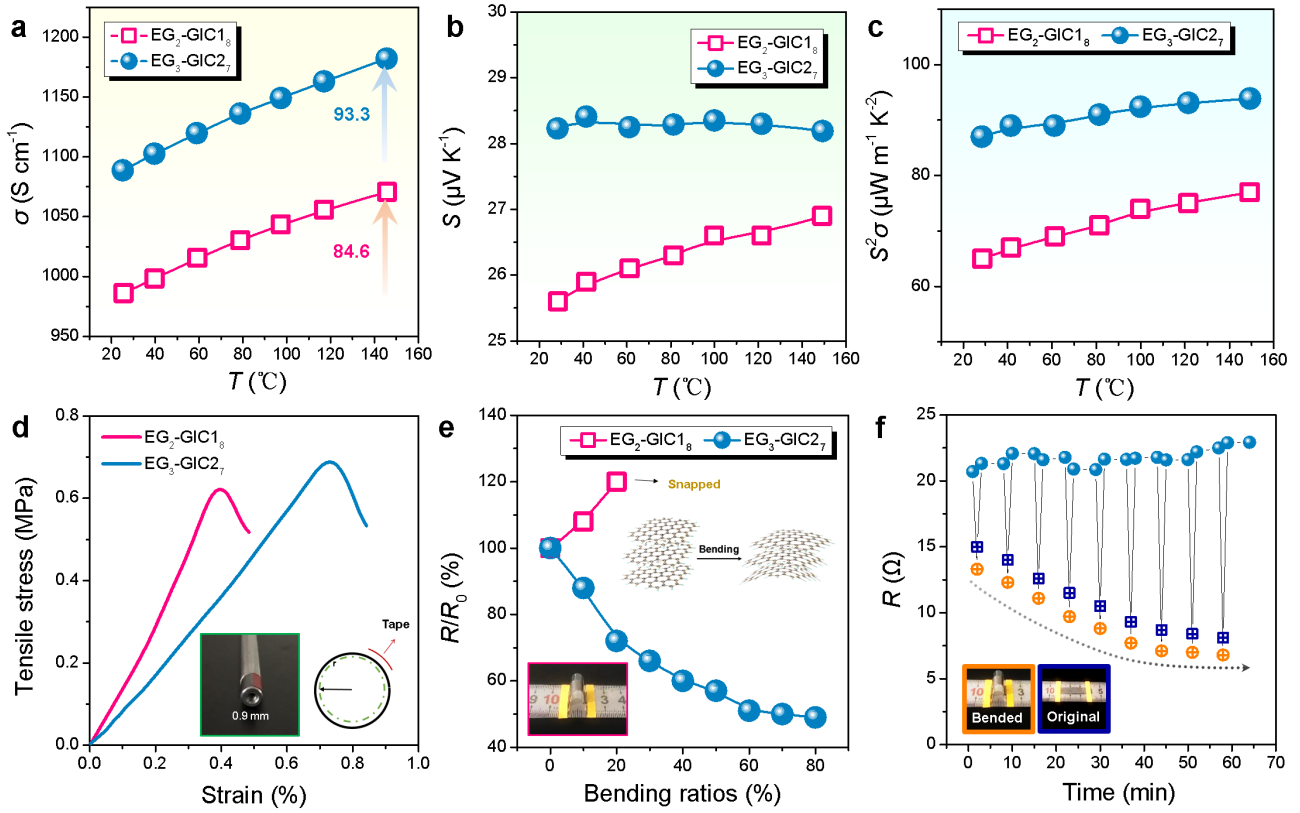


**Figure 4.** Temperature-dependent (a)  $\sigma$ , (b)  $S$ , and (c)  $S^2\sigma$  of EG<sub>2</sub>-GIC<sub>18</sub> and EG<sub>3</sub>-GIC<sub>27</sub>, (d) Tensile curves of EG<sub>2</sub>-GIC<sub>18</sub> and EG<sub>3</sub>-GIC<sub>27</sub>, (e)  $R/R_0$  of EG<sub>2</sub>-GIC<sub>18</sub> and EG<sub>3</sub>-GIC<sub>27</sub> under varies bending ratios, and (f) Resistance of EG<sub>3</sub>-GIC<sub>27</sub> under various bending times.

**2.4. Fabrication and application of the TE devices.** In order to investigate the practical application potential of the as-prepared EG<sub>3</sub>-GIC<sub>27</sub> composite, two types of homemade devices were fabricated. As shown in **Figure 5a-d**, a homemade device utilizing PET film as the substrate was assembled as **Device-1**. The identical size of all EG<sub>3</sub>-GIC<sub>27</sub> pieces is 3.5×1.0 cm<sup>2</sup>. Cu tapes were used for the fixing of all EG<sub>3</sub>-GIC<sub>27</sub> cells and delicate platinum wires were adopted as conductive connections. This device was used as a wristband to harvest body heat where the human wrist was used as the heat source

and a sponge was taped on the reverse side of the cold end to isolate direct heat transfer (**Figure 5d**). As can be seen, the output open circuit voltage is 3.7 mV when temperatures of the hot end and the cold end are 36.1 and 32.2 °C ( $\Delta T = 3.9$  °C) (**Figure S6a and S6b**). As a flexible wearable electronic device, the stability of Device-1 was characterized where the open circuit voltages were listed in **Table S9** after bending. As can be seen, the open-circuit voltage value maintains considerable to be 3.47 mV (6.7 % decreased) bending 80 % and 3.56 mV (4.3 % decreased) after bending 30 % for 10 cycles. However, the open-circuit voltage fluctuation range widens gradually as the bending progressed.

As well, a distinguished thermoelectric sensor (**Device-2**) was designed ultimately in this work using EG<sub>3</sub>-GIC<sub>27</sub> as the raw material, as shown in **Figure 5e-j**. In order to handle protean application conditions, a highly transparent (as demonstrated in **Figure 5e**), super flexible (completely scrollable as shown in the interposed picture of **Figure 5g**), and fully sealed device was prepared. Constituted with twelve and a half pieces of 5.0×0.5 cm<sup>2</sup> EG<sub>3</sub>-GIC<sub>27</sub> principal components, copper wire was adopted as the connection part, silver glue was used to fix the EG<sub>3</sub>-GIC<sub>27</sub> pieces and silica gel was potted ultimately to achieve comprehensive device protection (**Figure 5g**). This silica gel surfaced device was also characterized with adhesive feature which can be pasted on smooth implements conveniently such as refrigerator, reaction kettle, etc., as revealed in **Figure 5f and 5h**.<sup>61</sup> The output open-circuit voltage is 0.65 mV when the device was stuck on the cellphone back shell ( $\Delta T = 0.4$  °C as confirmed in **Figure S6c and S6d**) as shown in **Figure 5i**. As can be seen, the output open-circuit voltage is 1.33 mV when the intermediate section of the device was submerged in the river water whereas two side edges were exposed to the air ( $\Delta T = 1.6$  °C). Similarly, the open circuit voltages of Device-2 were listed in **Table S10** where better stability is obtained compared with Device-1. Open circuit voltage decreases by 3.1 % and 1.5 % after 80 % bent and 30 % bent for 10 cycles respectively.

It is worthy to fabricate entirely potted devices under moisture, blisters, or corrosive service environments. Besides, the excellent flexibility, silica gel tactile impression, and self-adhesive properties promise high potentials in the aspect of artificial electronic human skin.

In order to identify the power density of the as-designed devices, we used the methods developed in the previously report.<sup>62</sup> The external resistances of the as-designed devices were measured by a digital multimeter to be 683  $\Omega$  (Device-1) and 96  $\Omega$  (Device-2). The voltage on the external variable resistor as a function of external resistance is shown in **Figure S7**. As the output power is maximized when the external resistance equals the resistance of the device. The peak output power density can be calculated to be  $\sim 0.048 \mu\text{W cm}^{-2}$  with a temperature difference of 3.9  $^{\circ}\text{C}$  for Device-1. Similarly, the peak output power density can be calculated to be  $\sim 0.059 \mu\text{W cm}^{-2}$  with a temperature difference of 1.33  $^{\circ}\text{C}$  for Device-2. The lower internal resistance and high output power density of Device-2 confirm the advance of our device design.

Our conventional carbon-based composite emphasizes on the low-cost and large-scale fabrication of flexible thermoelectric materials. However, the thermoelectric properties are potential to be further improved by hybridization with conductive polymers, which is featured with excellent flexibility and qualified thermoelectric properties. Additionally, a new strategy to regulate the intercalation of GIC will also contribute to the optimization of the Seebeck coefficient.<sup>63</sup> Using these effective methods to further improve the thermoelectric performance and the flexibility of our material can expand the research attention and the practical value of our material in the future.

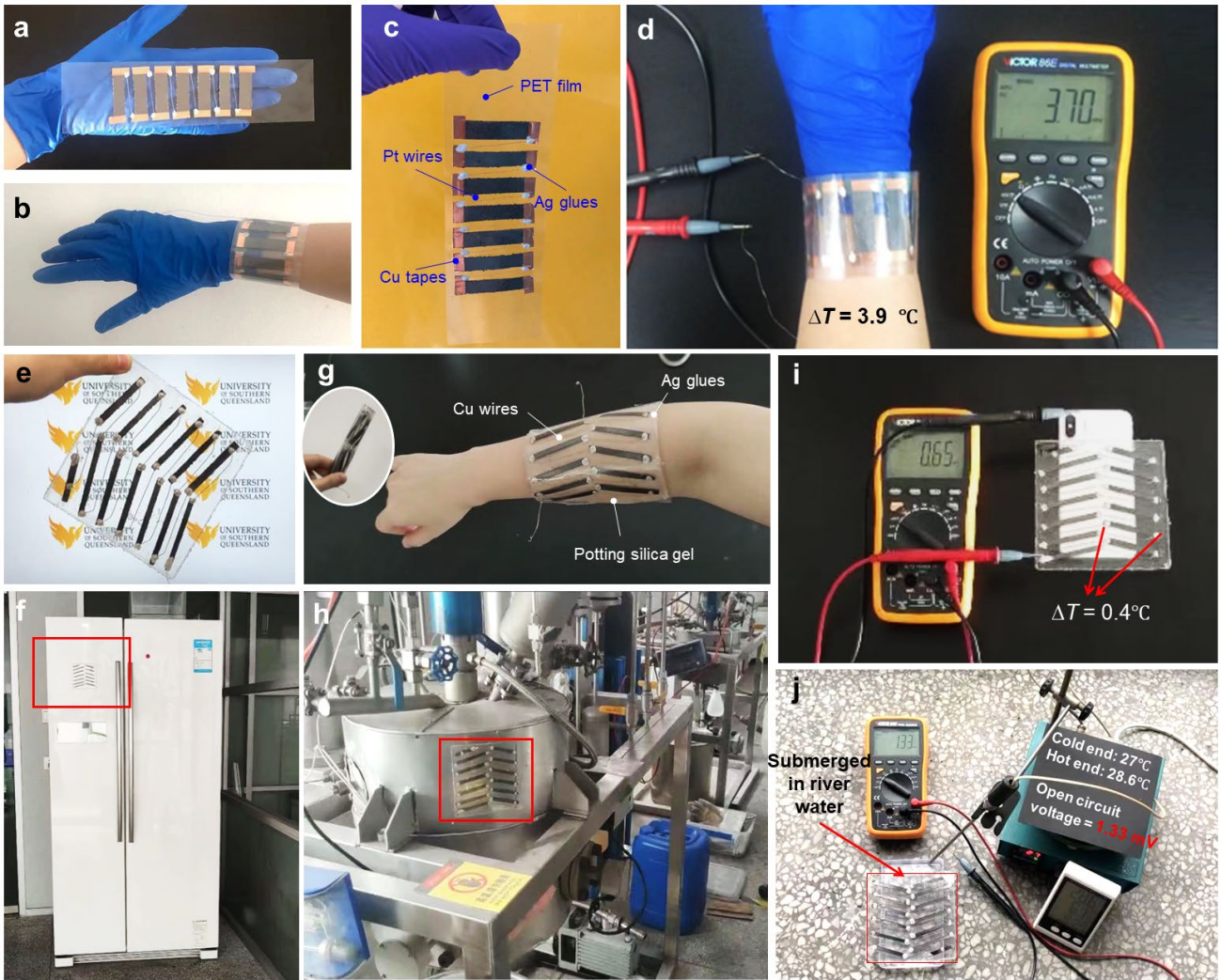


**Figure 5.** (a-d) Homemade thermoelectric device with PET matrix, and (e-j) Homemade thermoelectric device with plotted silica gel for protection.

### 3. CONCLUSION

In this study, a thermoelectric composite based on commercially conventional carbon materials has been designed and fabricated with a super promising 10-minute preparing cycle. More importantly, ten pieces of batch outputs produced by industrial equipment are provided in this work proving the material practicality and mass production operability. For the optimal blended specimen, namely EG<sub>3</sub>-GIC<sub>27</sub>, high  $\sigma$  of 1089 S cm<sup>-1</sup>,  $S$  of 28.2  $\mu$ V K<sup>-1</sup>, and  $S^2\sigma$  of 87  $\mu$ W m<sup>-1</sup> K<sup>-2</sup> are obtained at room

temperature. Subsequently, temperature-dependent thermoelectric performances shows a maximum  $S^2\sigma$  of  $94 \mu\text{W m}^{-1} \text{K}^{-2}$  at  $150 \text{ }^\circ\text{C}$  referring to EG<sub>3</sub>-GIC<sub>27</sub>. The entire procedure of preparation needs only 10 minutes and super high cost-effectiveness of  $7250 \mu\text{W g m}^{-1} \text{K}^{-2} \text{\$}^{-1}$  ( $S^2\sigma/\text{Cost}$  value) is achieved. Besides, two homemade devices were installed obtaining satisfied power generation in diverse application scenarios. Output open-circuit voltage reaches  $3.70 \text{ mV}$  using human wrist as the heat source ( $\Delta T = 3.9 \text{ }^\circ\text{C}$ ), and  $1.33 \text{ mV}$  output open-circuit voltage is generated when submerging the device directly into the river water ( $\Delta T = 1.6 \text{ }^\circ\text{C}$ ).

Notably, thermoelectric properties in this work are entirely obtained by facile prepared undoped composites. In the case of modification with advanced typical thermoelectric materials, performance is likely to be further boosted. Moreover, due to the high flexibility, advanced efficiency, excellent economy, and pioneered commerciality of the prepared composites, the preparing strategy provided in this work is significantly meaningful for the large-scale industrialization of thermoelectric materials.

## 4. EXPERIMENTAL SECTION

**4.1. Materials.** Commercial expanded graphite (industrial grade, 99%), graphite intercalation on compounds with 90 and 170 mesh (sulfuric acid and nitric acid intercalated, industrial grade, 99%) were purchased from Qingdao Dong Kai Carbon Co., Ltd. (Shandong, China). Herein, GIC1 refers to the 170 mesh GIC particles, and GIC2 refers to the 90 mesh GIC particles. Moreover, the substrate PET films were supplied by Wuxi HIT New Material Research Institute Co., Ltd. (Wuxi, China). Encapsulation material silica gels were supplied by Jiangxi Bluestar Xinghuo Silicone Co., Ltd. (Jiangxi, China).

Hot pressing of the EG-GIC composite films: EG-GIC composite films were fabricated by a facile

one-step hot-pressing method in accordance with the standard industrial hot pressing process, as illustrated by **Figure 1b**. EG and GIC were proportionally weighed and dried in an oven under 105 °C for 3 h. Subsequently, the dewatered powder mixtures were uniformly mechanically mixed in a blade shredder. After spreading in a flat stainless steel mould (7.5×5.0 cm<sup>2</sup> model acreage), hot tableting was carried out via a flat vulcanizer in the condition of 70 °C, 12 MPa (confirmed by **Table S11**), and maintained for 5 min. The thicknesses of all obtained thin films were regulated at ~0.3 mm. Further, industrial simulations were conducted using a larger mould with 25×20 cm<sup>2</sup> surface area and ten pieces of mass productions were obtained, as illustrated in **Figure 1c**. The density of all specimens demonstrates an interval of 1.45±0.02 g cm<sup>-3</sup> by Archimedes method.

**4.2. Fabrication of thermoelectric Device-1 with PET substrate.** The as-prepared EG<sub>3</sub>-GIC<sub>27</sub> thin films were cut into rectangular pieces with identical sizes of 3.5×1.0 cm<sup>2</sup>. Seven pieces of rectangular units were alloyed and pasted on the PET film with copper tapes. Afterward, separated pieces are connected end-to-end using platinum wires. Another layer of PET film was then covered as the top layer for protection, and the homemade thermoelectric bracelet was completed followed by taping a piece of sponge to the cold end, which serves as the insulation unit. **Device-1** benefits with the advantage of the rapid body heat transfer via PET thin film which results in larger  $\Delta T$ .

**4.3. Fabrication of thermoelectric Device-2 with silica gel encapsulation.** Similar processes were conducted where twelve and a half pieces of 5.0×0.5 cm<sup>2</sup> EG<sub>3</sub>-GIC<sub>27</sub> thin films were alloyed slantwise and connected end-to-end through silver glue and copper wire. Then the system was potted by silica gels through a tetrafluoroethylene mould. **Device-2** benefits with great capabilities of self-adhesive and water resistance despite the major drawback of the inferior heat transfer speed and smaller  $\Delta T$ .

**4.4. Characterizations.** Particle sizes of the mixed EG-GIC powders were measured by a laser particle size instrument (MS 2000, UK) using deionized water as the dispersion medium. All  $\sigma$  and  $S$  were determined using a SBA 458 (NETZSCH, Germany) under helium atmosphere, **with sample sizes listed in Table S12.** Raman spectrometer (HORIBA Labram HR Evolution, Japan) was used to characterize the ordering degree of the multi-layered composites. **Hall coefficients and carrier concentrations were measured by the the Van der Pauw method (F-50, CH-Hall Electronic, China).** Vertical thermal X-ray diffraction (XRD, D8 Advance, Germany) analysis was performed at room temperature using Cu  $K_{\alpha}$  radiation source to investigate the crystal structure. X-ray photoemission spectroscopy (XPS, Thermo Scientific K-Alpha, USA) was carried out to analyze the element compositions. Micro-morphologies of the composites were detected by scanning electron microscopy (SEM, Hitachi TM3000, Japan) equipped with an energy dispersive X-ray spectrometer (EDS). Tensile strength and elongation at break were measured by a universal testing machine (Instron E44, USA) at a tensile speed of  $5 \text{ mm min}^{-1}$  after cutting into dumbbell-like models of the specimens.

## ASSOCIATED CONTENT

### Supporting Information

The Supporting Information is available free of charge at DOI:

Enlarged XRD spetras highlighting the (002) diffraction peaks, TE properties ( $\sigma$ ,  $S$ , and  $S^2\sigma$ ) of EG<sub>3</sub>-GIC<sub>27</sub> under as-prepared status and afer exposed in the air for 180 days, arbitrary shaping images of EG<sub>3</sub>-GIC<sub>27</sub>, temperature measurement of the hot side and cold side in conditions, comparison of thermoelectric properties and prices of the as-prepared composite EG<sub>3</sub>-GIC<sub>27</sub> and some typical flexible thermoelectric materials reported in literature, preliminary experiment

results of thermoelectric properties of different as-prepared commercial-carbon based composite materials, detailed XRD characteristic parameters, and detailed element content ratios provided by XPS measurements.

## AUTHOR INFORMATION

### Corresponding Authors

**Zhi-Gang Chen** - *Centre for Future Materials, University of Southern Queensland, Springfield Central, Queensland 4300, Australia; School of Chemistry and Physics, Queensland University of Technology, Brisbane City QLD 4000, Australia; \*E-mail: [zhigang.chen@qut.edu.au](mailto:zhigang.chen@qut.edu.au)*

**Qingfeng Liu** - *State Key Laboratory of Materials Oriented Chemistry Engineering, College of Chemistry Engineering, Nanjing Tech University, Nanjing 211800, China; \*E-mail: [qfliu@njtech.edu.cn](mailto:qfliu@njtech.edu.cn)*

### Authors

**Shuai Sun** - *Centre for Future Materials, University of Southern Queensland, Springfield Central, Queensland 4300, Australia*

**Xiao-Lei Shi** - *Centre for Future Materials, University of Southern Queensland, Springfield Central, Queensland 4300, Australia; School of Chemistry and Physics, Queensland University of Technology, Brisbane City QLD 4000, Australia*

**Wei-Di Liu** - *Centre for Future Materials, University of Southern Queensland, Springfield Central, Queensland 4300, Australia*

**Ting Wu** - *State Key Laboratory of Materials Oriented Chemistry Engineering, College of Chemistry Engineering, Nanjing Tech University, Nanjing 211800, China*

**Dezhuang Wang** - *State Key Laboratory of Materials Oriented Chemistry Engineering, College of Chemistry Engineering, Nanjing Tech University, Nanjing 211800, China*

**Hao Wu** - *State Key Laboratory of Materials Oriented Chemistry Engineering, College of Chemistry Engineering, Nanjing Tech University, Nanjing 211800, China*

**Xiaoyong Zhang** - *School of Materials Science and Engineering, Anhui University of Science and Technology, Huainan 232001, China*

**Yu Wang** - *Jiangxi Bluestar Xinghuo Silicone Co., Ltd., Jiujiang 330319, China*

### **Author Contributions**

The manuscript was written through contributions of all authors. All authors have given approval to the final version of the manuscript.

### **Notes**

The authors declare no competing financial interest.

### **ACKNOWLEDGEMENTS**

This work was financially supported by the Australian Research Council and Innovation Centre for Sustainable Steel Project. The authors acknowledge the facilities, and the scientific and technical assistance, of the Australian Microscopy & Microanalysis Research Facility at the Centre for Microscopy and Microanalysis, The University of Queensland. **QF Liu thanks the financial support**

from the National Natural Science Foundation of China (No. 51972170). The authors express gratitude to Liangchuang Zhai and Liangcao Yin for providing help to accomplish this work.

## REFERENCES

- (1) Xiao, Y.; Zhao, L. D. Seeking New, Highly Effective Thermoelectrics. *Science* **2020**, *367*, 1196-1197.
- (2) Jiang, B.; Yu, Y.; Cui, J.; Liu, X.; Xie, L.; Liao, J.; Zhang, Q.; Huang, Y.; Ning, S.; Jia, B.; Zhu, B.; Bai, S.; Chen, L.; Pennycook, S. J.; He, J. High-Entropy-Stabilized Chalcogenides with High Thermoelectric Performance. *Science* **2021**, *371*, 830-834.
- (3) Xu, Y.; Xu, P.; Hu, D.; Ma, Y. Recent Progress in Hot Exciton Materials for Organic Light-Emitting Diodes. *Chem. Soc. Rev.* **2021**, *50*, 1030-1069.
- (4) Shi, X.; Chen, L. Thermoelectric Materials Step Up. *Nat. Mater.* **2016**, *15*, 691-692.
- (5) Wu, J.; Sun, Y.; Xu, W.; Zhang, Q. Investigating Thermoelectric Properties of Doped Polyaniline Nanowires. *Synth. Met.* **2014**, *189*, 177-182.
- (6) Zhang, L.; Shi, X.-L.; Yang, Y.-L.; Chen, Z.-G. Flexible Thermoelectric Materials and Devices: From Materials to Applications. *Mater. Today* **2021**, *46*, 62-108.
- (7) Shi, X. L.; Zou, J.; Chen, Z. G. Advanced Thermoelectric Design: From Materials and Structures to Devices. *Chem. Rev.* **2020**, *120*, 7399-7515.
- (8) Xu, S.; Shi, X.-L.; Dargusch, M.; Di, C.; Zou, J.; Chen, Z.-G. Conducting Polymer-Based Flexible Thermoelectric Materials and Devices: From Mechanisms to Applications. *Prog. Mater. Sci.* **2021**, *121*,

100840.

(9) Shi, X.-L.; Chen, W.-Y.; Zhang, T.; Zou, J.; Chen, Z.-G. Fiber-Based Thermoelectrics for Solid, Portable, and Wearable Electronics. *Energ. Environ. Sci.* **2021**, *14*, 729-764

(10) Zhao, W.; Ding, J.; Zou, Y.; Di, C. A.; Zhu, D. Chemical Doping of Organic Semiconductors for Thermoelectric Applications. *Chem. Soc. Rev.* **2020**, *49*, 7210-7228.

(11) Xu, S.; Hong, M.; Shi, X.; Li, M.; Sun, Q.; Chen, Q.; Dargusch, M.; Zou, J.; Chen, Z.-G. Computation-Guided Design of High-Performance Flexible Thermoelectric Modules for Sunlight-to-Electricity Conversion. *Energ. Environ. Sci.* **2020**, *13*, 3480-3488.

(12) Wu, J.; Hu, R.; Zeng, S.; Xi, W.; Huang, S.; Deng, J.; Tao, G. Flexible and Robust Biomaterial Microstructured Colored Textiles for Personal Thermoregulation. *ACS Appl. Mater. Inter.* **2020**, *12*, 19015-19022.

(13) Liu, W.; Yan, X.; Chen, G.; Ren, Z. Recent Advances in Thermoelectric Nanocomposites. *Nano Energy* **2012**, *1*, 42-56.

(14) Wei, T.-R.; Guan, M.; Yu, J.; Zhu, T.; Chen, L.; Shi, X. How to Measure Thermoelectric Properties Reliably. *Joule* **2018**, *2*, 2183-2188.

(15) Bharti, M.; Singh, A.; Samanta, S.; Aswal, D. K. Conductive Polymers for Thermoelectric Power Generation. *Prog. Mater. Sci.* **2018**, *93*, 270-310.

(16) Kim, G. H.; Shao, L.; Zhang, K.; Pipe, K. P. Engineered Doping of Organic Semiconductors for Enhanced Thermoelectric Efficiency. *Nat. Mater.* **2013**, *12*, 719-723.

(17) Yao, C. J.; Zhang, H. L.; Zhang, Q. Recent Progress in Thermoelectric Materials Based on

Conjugated Polymers. *Polymers (Basel)* **2019**, *11*, 107.

(18) Cao, T.; Shi, X.-L.; Zou, J.; Chen, Z.-G. Advances in Conducting Polymer-based Thermoelectric Materials and Devices. *Microstructures* **2021**, *1*, 2021007.

(19) Zhao, W.; Fan, S.; Xiao, N.; Liu, D.; Tay, Y. Y.; Yu, C.; Sim, D.; Hng, H. H.; Zhang, Q.; Boey, F.; Ma, J.; Zhao, X.; Zhang, H.; Yan, Q. Flexible Carbon Nanotube Papers with Improved Thermoelectric Properties. *Energ. Environ. Sci.* **2012**, *5*, 5364-5369

(20) Dragoman, D.; Dragoman, M. Giant Thermoelectric Effect in Graphene. *Appl. Phys. Lett.* **2007**, *91*, 203116.

(21) Perez-Taborda, J. A.; Caballero-Calero, O.; Vera-Londono, L.; Briones, F.; Martin-Gonzalez, M. High Thermoelectric  $zT$  in n-Type Silver Selenide Films at Room Temperature. *Adv. Energ. Mater.* **2018**, *8*, 1702024.

(22) Wei, T. R.; Jin, M.; Wang, Y.; Chen, H.; Gao, Z.; Zhao, K.; Qiu, P.; Shan, Z.; Jiang, J.; Li, R.; Chen, L.; He, J.; Shi, X. Exceptional Plasticity in the Bulk Single-Crystalline van der Waals Semiconductor InSe. *Science* **2020**, *369*, 542-545.

(23) Ibanez, M.; Luo, Z.; Genc, A.; Piveteau, L.; Ortega, S.; Cadavid, D.; Dobrozhan, O.; Liu, Y.; Nachtegaal, M.; Zebarjadi, M.; Arbiol, J.; Kovalenko, M. V.; Cabot, A. High-performance Thermoelectric Nanocomposites from Nanocrystal Building Blocks. *Nat. Commun.* **2016**, *7*, 10766.

(24) Wang, Z. H.; Ichimura, K.; Dresselhaus, M. S.; Dresselhaus, G.; Lee, W.; Wang, K. A.; Eklund, P. C. Electronic Transport Properties of  $K_xC_{70}$  Thin Films. *Phys. Rev. B* **1993**, *48*, 10657-10660.

(25) Zhang, Y.; Zhang, Q.; Chen, G. Carbon and Carbon Composites for Thermoelectric Applications.

*Carbon Energy* **2020**, *2*, 408-436.

(26) Sheng, M.; Wang, Y.; Liu, C.; Xiao, Y.; Zhu, P.; Deng, Y. Significantly Enhanced Thermoelectric Performance in SWCNT Films via Carrier Tuning for High Power Generation. *Carbon* **2020**, *158*, 802-807.

(27) Choi, J.; Jung, Y.; Dun, C.; Park, K. T.; Gordon, M. P.; Haas, K.; Yuan, P.; Kim, H.; Park, C. R.; Urban, J. J. High-Performance, Wearable Thermoelectric Generator Based on a Highly Aligned Carbon Nanotube Sheet. *ACS Appl. Energ. Mater.* **2019**, *3*, 1199-1206.

(28) Gao, J.; Liu, C.; Miao, L.; Wang, X.; Peng, Y.; Chen, Y. Enhanced Power Factor in Flexible Reduced Graphene Oxide/Nanowires Hybrid Films for Thermoelectrics. *RSC Adv.* **2016**, *6*, 31580-31587.

(29) Novak, T. G.; Kim, J.; Kim, J.; Shin, H.; Tiwari, A. P.; Song, J. Y.; Jeon, S. Flexible Thermoelectric Films with High Power Factor Made of Non-oxidized Graphene Flakes. *2D Mater.* **2019**, *6*, 045019.

(30) Chung, D. D. L. Electromagnetic Interference Shielding Effectiveness of Carbon Materials. *Carbon* **2001**, *39*, 279-285.

(31) Akbari, A.; Cunning, B. V.; Joshi, S. R.; Wang, C.; Camacho-Mojica, D. C.; Chatterjee, S.; Modepalli, V.; Cahoon, C.; Bielawski, C. W.; Bakharev, P.; Kim, G. -H.; Ruoff, R. S. Highly Ordered and Dense Thermally Conductive Graphitic Films from a Graphene Oxide/Reduced Graphene Oxide Mixture. *Matter* **2020**, *2*, 1198-1206.

(32) Li, J.-h.; Feng, L.-l.; Jia, Z.-x. Preparation of Expanded Graphite with 160  $\mu\text{m}$  mesh of Fine Flake Graphite. *Mater. Lett.* **2006**, *60*, 746-749.

- (33) Park, J.; Xu, Z. L.; Yoon, G.; Park, S. K.; Wang, J.; Hyun, H.; Park, H.; Lim, J.; Ko, Y. J.; Yun, Y. S.; Kang, K. Stable and High-Power Calcium-Ion Batteries Enabled by Calcium Intercalation into Graphite. *Adv. Mater.* **2020**, *32*, e1904411.
- (34) Dhakate, S.; Sharma, S.; Borah, M.; Mathur, R.; Dhami, T. Expanded Graphite-based Electrically Conductive Composites as Bipolar Plate for PEM Fuel Cell. *Int. J. Hydrogen Energ.* **2008**, *33*, 7146-7152.
- (35) Wang, C. Y.; Li, H. R.; Qin, C. L.; Zhang, P. Preparation of Low-Sulfur Expanded Graphite with Different Size Particles. *Adv. Mater. Res.* **2013**, *652-654*, 745-748.
- (36) Liu, W.-D.; Yu, Y.; Dargusch, M.; Liu, Q.; Chen, Z.-G. Carbon Allotrope Hybrids Advance Thermoelectric Development and Applications. *Renew. Sust. Energ. Rev.* **2021**, *141*, 110800.
- (37) Wei, J.; Li, X.; Wang, Y.; Chen, B.; Qiao, S.; Zhang, Q.; Xue, F. Record High Thermoelectric Performance of Expanded Graphite/Carbon Fiber Cement Composites Enhanced by Ionic Liquid 1-butyl-3-methylimidazolium Bromide for Building Energy Harvesting. *J. Mater. Chem. C* **2021**, *9*, 3682-3691.
- (38) Benthien, J. T.; Thoemen, H. Effects of Agglomeration and Pressing Process on the Properties of Flat Pressed WPC Panels. *J. Appl. Polym. Sci.* **2013**, *129*, 3710-3717.
- (39) Wei, H.; Cao, P. X.; Guo, X. L.; Wang, B. J.; Qiao, Z. M.; Hu, W. Design of Blank Thickness on-Line Monitoring System of Continuous Flat Press in Wood-Based Panel Industry. *Appl. Mech. Mater.* **2011**, *130-134*, 3767-3772.
- (40) Mase, K. Abrasive for Blast Processing and Blast Processing Method Employing the Same. **2012**,

US.

(41) Cheng, H.; He, X.; Fan, Z.; Ouyang, J. Flexible Quasi-Solid State Ionogels with Remarkable Seebeck Coefficient and High Thermoelectric Properties. *Adv. Energ. Mater.* **2019**, *9*, 1901085.

(42) Zheng, Y.-P.; Wang, H.-N.; Kang, F.-Y.; Wang, L.-N.; Inagaki, M. Sorption Capacity of Exfoliated Graphite for Oils-sorption in and among Worm-Like Particles. *Carbon* **2004**, *42*, 2603-2607.

(43) Brandt, A. M.; Józwiak-Niedźwiedzka, D. Diagnosis of Concrete Quality by Structural Analysis. *Adv. Civil Eng. Mater.* **2012**, *1*, 20120004.

(44) Zhang, Y.; Rhee, K. Y.; Park, S.-J. Facile Design of a Domestic Thermoelectric Generator by Tailoring the Thermoelectric Performance of Volume-Controlled Expanded Graphite/PVDF Composites. *Compos. Part B: Eng.* **2019**, *176*, 107234.

(45) Focke, W. W.; Badenhorst, H.; Mhike, W.; Kruger, H. J.; Lombaard, D. Characterization of Commercial Expandable Graphite Fire Retardants. *Thermochim. Acta* **2014**, *584*, 8-16.

(46) Shin, Y.-R.; Jung, S.-M.; Jeon, I.-Y.; Baek, J.-B. The Oxidation Mechanism of Highly Ordered Pyrolytic Graphite in a Nitric Acid/Sulfuric Acid Mixture. *Carbon* **2013**, *52*, 493-498.

(47) Slade, T. J.; Anand, S.; Wood, M.; Male, J. P.; Imasato, K.; Cheikh, D.; Al Malki, M. M.; Agne, M. T.; Griffith, K. J.; Bux, S. K.; Wolverton, C.; Kanatzidis, M. G.; Snyder, G. J. Charge-Carrier-Mediated Lattice Softening Contributes to High zT in Thermoelectric Semiconductors. *Joule* **2021**, *5*, 1168-1182.

(48) Malard, L. M.; Pimenta, M. A.; Dresselhaus, G.; Dresselhaus, M. S. Raman Spectroscopy in Graphene. *Phys. Rep.* **2009**, *473*, 51-87.

- (49) Pan, C.; Zhang, L.; Pan, Z.; Chen, M.; Liu, Y.; Huang, G.; Na, H.; Wang, W.; Qiu, H.; Gao, J. A Simple Strategy to Fabricate Polyaniline/Expanded Graphite Composites with Improved Power Factor. *Mater. Chem. Phys.* **2015**, *167*, 315-319.
- (50) Wang, G.; Wang, F.; Zhang, P.; Zhang, J.; Zhang, T.; Mullen, K.; Feng, X. Polarity-Switchable Symmetric Graphite Batteries with High Energy and High Power Densities. *Adv. Mater.* **2018**, *30*, e1802949.
- (51) Dresselhaus, M. S.; Dresselhaus, G. Intercalation Compounds of Graphite. *Adv. Phys.* **2002**, *51*, 1-186.
- (52) Liu, S.; Zhang, Y.; Ge, B.; Zheng, F.; Zhang, N.; Zuo, M.; Yang, Y.; Chen, Q. Constructing Graphitic-Nitrogen-Bonded Pentagons in Interlayer-Expanded Graphene Matrix toward Carbon-Based Electrocatalysts for Acidic Oxygen Reduction Reaction. *Adv. Mater.* **2021**, *33*, e2103133.
- (53) Greczynski, G.; Hultman, L. The Same Chemical State of Carbon Gives Rise to Two Peaks in X-ray Photoelectron Spectroscopy. *Sci. Rep.* **2021**, *11*, 11195.
- (54) Fareed, M. A.; Stamboulis, A. Nanoclays Reinforced Glass Ionomer Cements: Dispersion and Interaction of Polymer Grade (PG) Montmorillonite with Poly(acrylic acid). *J. Mater. Sci. Mater. Med.* **2014**, *25*, 91-99.
- (55) Xiao, H.-Z.; Xiao, B.; Wu, H.-H. Interfacial Characteristics and Mechanical Properties of the Vacuum Brazing Diamond Grains Segment with Ni-Cr Composite Active Filler and Tungsten Carbide Reinforcement. *J. Alloy. Compd.* **2019**, *781*, 226-234.
- (56) Wang, S.; Xiao, Y.; Ren, D.; Su, L.; Qiu, Y.; Zhao, L.-D. Enhancing Thermoelectric Performance

of BiSbSe<sub>3</sub> through Improving Carrier Mobility via Percolating Carrier Transports. *J. Alloy. Compd.* **2020**, *836*, 155473.

(57) Bubnova, O.; Khan, Z.; Malti, A.; Braun, S.; Fahlman, M.; Berggren, M.; Crispin, X. Optimization of the Thermoelectric Figure of Merit in the Conducting Polymer Poly(3,4-ethylenedioxythiophene). *Nature Mater.* **2011**, *10*, 429-433.

(58) Kee, S.; Kim, H.; Paleti, S. H. K.; Labban, A. E.; Neophytou, M.; Emwas, A.-H.; Alshareef, H. N.; Baran, D. Highly Stretchable and Air-Stable PEDOT:PSS/Ionic Liquid Composites for Efficient Organic Thermoelectrics. *Chem. Mater.* **2019**, *31*, 3519-3526.

(59) Li, F.; Wei, T.-R.; Kang, F.; Li, J.-F. Thermoelectric Properties of BiCuSeO with Bismuth and Oxygen Vacancies. *J. Alloy. Compd.* **2014**, *614*, 394-400.

(60) Zhang, M.; Wang, C.; Wang, H.; Jian, M.; Hao, X.; Zhang, Y. Carbonized Cotton Fabric for High-Performance Wearable Strain Sensors. *Adv. Funct. Mater.* **2017**, *27*, 1604795.

(61) Vázquez, A. V.; Boughton, A. P.; Shephard, N. E.; Rhodes, S. M.; Chen, Z. Molecular Structures of the Buried Interfaces between Silicone Elastomer and Silane Adhesion Promoters Probed by Sum Frequency Generation Vibrational Spectroscopy and Molecular Dynamics Simulations. *ACS Appl. Mater. Inter.* **2009**, *2*, 96-103.

(62) Xu, S.; Hong, M.; Shi, X.-L.; Wang, Y.; Ge, L.; Bai, Y.; Wang, L.; Dargusch, M.; Zou, J.; Chen, Z.-G. High-Performance PEDOT:PSS Flexible Thermoelectric Materials and Their Devices by Triple Post-Treatments. *Chem. Mater.* **2019**, *31*, 5238-5244

(63) Matsumoto, R.; Okabe, Y.; Akuzawa, N. Thermoelectric Properties and Performance of n-type

and p-type Graphite Intercalation Compounds. *J. Electron. Mater.* **2015**, *44*, 399-406.

# Table of Contents

